



Bifunctional integrated electrode for high-efficient hydrogen production coupled with 5-hydroxymethylfurfural oxidation

Yuke Song^a, Wenfu Xie^{a,*}, Yingjie Song^a, Hao Li^b, Shijin Li^a, Shan Jiang^a, Jin Yong Lee^b, Mingfei Shao^{a,*}

^a State Key Laboratory of Chemical Resource Engineering, Beijing University of Chemical Technology, Beijing 100029, China

^b Department of Chemistry, Sungkyunkwan University, Suwon 16419, South Korea



ARTICLE INFO

Keywords:

Hydrogen evolution
Integrated electrode
Biomass oxidation
Transition-metal phosphides
Coupled oxidation

ABSTRACT

The sluggish oxygen evolution reaction (OER) limits the efficiency of overall water splitting, which thereby hinders hydrogen evolution reaction (HER). Here, we demonstrate a bifunctional CoNiP nanosheet integrated electrode (CoNiP-NIE) to boost HER and replace OER by 5-hydroxymethylfurfural oxidation reaction (HMFOR) to obtain high-valued 2,5-furandicarboxylic acid (FDCA). The as-developed CoNiP-NIE exhibits a constant high Faradaic efficiency more than 82% for HMFOR in a wide potential from 1.40 V to 1.70 V vs. RHE, which stand at the top level among the reported electrocatalysts. Moreover, the low overpotential for HER further indicates its high efficiency in the H₂ generation. Based on the bifunctional activity of CoNiP, an electrochemical hydrogen evolution coupled with biomass oxidation device is constructed, which delivers lower voltage (1.46 V) for anode oxidation and higher evolution rate of H₂ (41.2 L h⁻¹ m⁻²) than water splitting (1.76 V, 16.1 L h⁻¹ m⁻²).

1. Introduction

As a clean and renewable energy resource, hydrogen, has been widely regarded as a promising alternative to replace the ever-diminishing fossil fuel [1,2]. Among various hydrogen production technologies, the electrochemical water splitting powered by clean energy has been considered as an efficient and prospective sustainable technology to gain high-purity hydrogen, but suffering from the kinetically sluggish anodic oxygen evolution reaction (OER) and less value-added O₂ [3]. Although with reduced overpotential of OER by developing advanced electrocatalysts, it still fails to achieve a qualitative breakthrough for overall reaction efficiency. Alternatively, exploiting novel anodic oxidation reactions with favorable thermodynamics and kinetics to couple with cathodic hydrogen evolution reaction (HER) provide a chance to reduce the cell voltage of electrolysis system [4–6]. For instance, the electrooxidation of alcohols (*e.g.*, methanol [7], ethanol [8]), hydrazine [9] and urea [10] have been widely adopted to promote the energy conversion efficiency. Even though above results are already quite successful, it is still challenging to boost hydrogen production and yield value-added chemical products with high selectivity simultaneously.

Recently, 5-hydroxymethylfurfural (HMF), a typical biomass-based

platform compounds, and its electrooxidation process have been extensively investigated [11–13]. One of oxidation products from HMF oxidation reaction (HMFOR), 2,5-furandicarboxylic acid (FDCA), increasingly arouse interest to be readily used as a monomer for producing important polymeric materials such as polyethylene furandicarboxylate [14]. Over the past decade, substantial advanced electrocatalysts, including precious metal [15], transition-metal oxides/hydroxides [16,17], transition-metal phosphides/sulfides [11,18], have been exploited for HMFOR. Among them, transition metal-based (Ni, Co and Fe) layered double hydroxides (LDHs) or oxyhydroxides draw researchers' attention due to their high activity, low cost and tunable composition [19]. For example, NiFe-LDH nanosheets on the carbon fiber paper were prepared for direct electrochemical HMFOR to produce FDCA with a Faraday efficiency (FE) of 99.4% at 1.23 V vs. reversible hydrogen electrode (RHE) [20]. Moreover, coupling HMFOR with HER can enhance the efficiency of hydrogen production in cathode by reducing the overpotential of anodic reaction. An ultrathin CoAl-LDH nanosheet array has been reported by *in-situ* electrochemical exfoliation method, which exhibits excellent performance for HMFOR with a low potential of 1.30 V vs. RHE at 10 mA cm⁻² and a high hydrogen production rate (44.16 L h⁻¹ m⁻²) [17]. However, because of inevitable OER, the FE of HMFOR to FDCA (FE_{FDCA}) on these catalysts

* Corresponding authors.

E-mail addresses: xiewf@mail.buct.edu.cn (W. Xie), shaomf@mail.buct.edu.cn (M. Shao).

usually drops sharply along with the increasing of oxidation potential (>1.50 V vs. RHE), resulting in a limited selectivity at high current density. Another key issue for HMFOR electrocatalysts is the poor HER performance, thus relying on additional electrocatalysts (normally Pt-based materials) to assemble the electrocatalysis system, which complicate the reaction system from the point view of practical application [2]. Hence, it will be much more desirable to catalyze the reaction in both anode and cathode simultaneously with a bifunctional electrocatalyst. Apart from this, constructing appropriate structure for catalysts to facilitate the diffusion of organic molecule in anode and the rapid leakage of gas in cathode also remain a major challenge [21]. Therefore, exploring and optimizing catalysts to match the reaction efficiency between anode and cathode towards large-scale hydrogen production still call for more efforts.

Herein, we report a bifunctional CoNiP nanosheet integrated electrode (CoNiP-NIE) by facile ion etching and subsequent phosphidation process, which shows promising activity for HMFOR and HER simultaneously (Fig. 1a). Typically, the CoNiP-NIE exhibits a high FE_{FDCA} of 87.2% at 1.50 vs. RHE and maintains basically stable (more than 82%) in a wide potential from 1.40 V to 1.70 V vs. RHE for HMFOR, and low overpotential of 107.56 mV at -10 mA cm^{-2} for HER, which

outperform most reported electrocatalysts. Moreover, a novel electrochemical hydrogen evolution coupled with biomass oxidation (ECHO) system for HMFOR and HER was constructed based on bifunctional CoNiP-NIE, which exhibits a low potential of 1.46 V at 20 mA cm^{-2} , accelerated evolution rate of H_2 ($41.2 \text{ L h}^{-1} \text{ m}^{-2}$) and high FDCA yield rate ($85.5 \text{ g h}^{-1} \text{ m}^{-2}$). The ECHO system can be driven by a commercial Si solar cell, which achieves 0.8% of solar-to-FDCA and 5.5% of solar-to- H_2 conversion efficiency. The dynamic structure change of CoNiP was detected by *in-situ* potential-dependent electrochemical impedance spectra (EIS) and Raman spectra, showing that CoNiP is firstly oxidized to metal oxyhydroxide and then metal oxyhydroxide is *in-situ* reduced by HMF during catalytic process. Theoretical calculations confirm that CoNiP with the enhanced electrical conductivity and moderate desorption of FDCA molecule account for the superior activity for HMFOR.

2. Experimental section

2.1. Synthesis of hierarchical CoNiP-NIE

Firstly, CoNi-LDH-NIE was synthesized using an optimized ion exchange/etching method reported by ZIF-67 nanoarray directly grown on

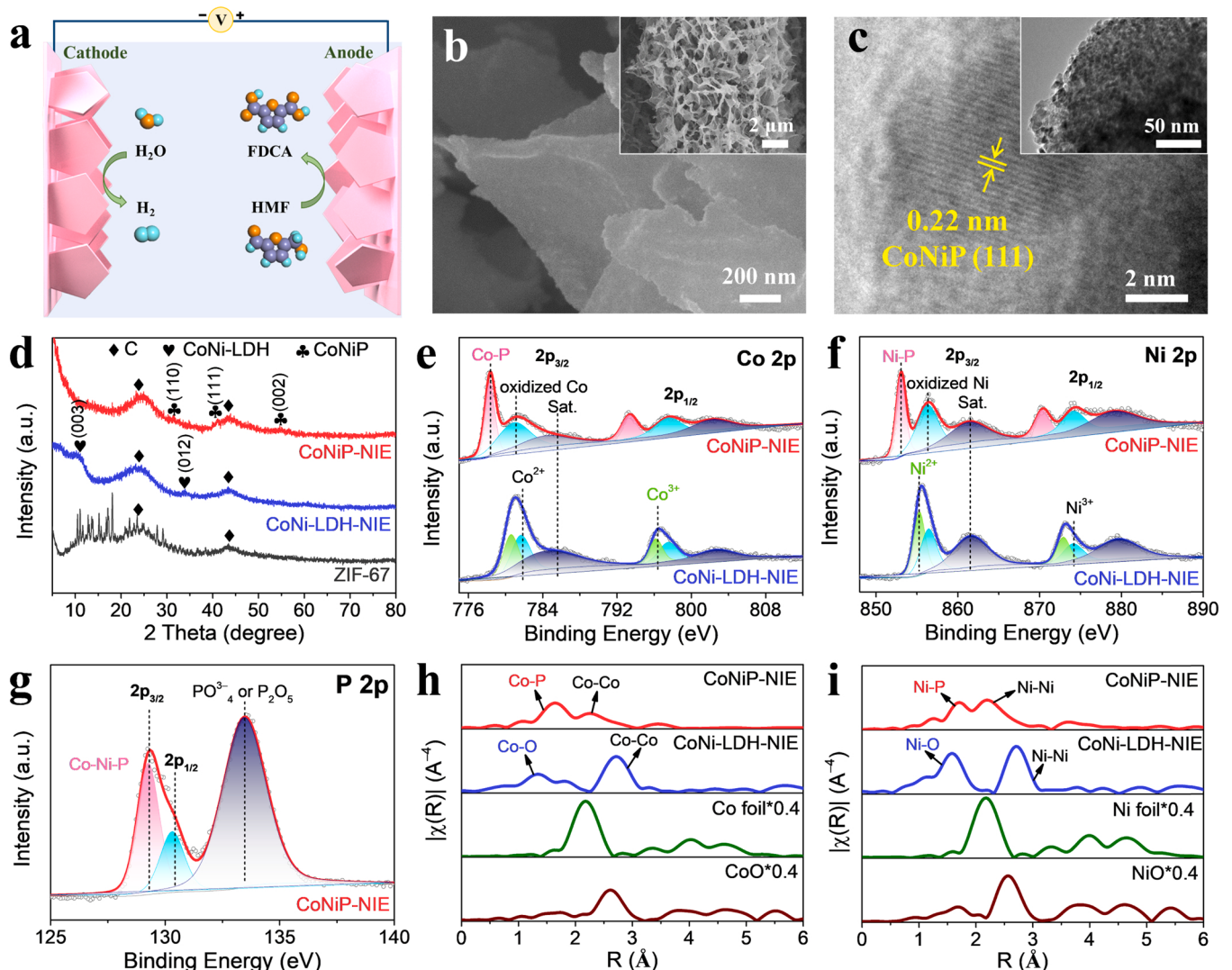


Fig. 1. (a) Schematic illustration of bifunctional CoNiP-NIE for HMFOR and HER. (b) SEM images of CoNiP-NIE. (c) TEM and high-resolution TEM (HRTEM, inset) images of CoNiP nanoarray. (d) XRD patterns of ZIF-67, CoNi-LDH-NIE and CoNiP-NIE. High-resolution XPS spectra of (e) Co 2p, (f) Ni 2p and (g) P 2p for CoNiP-NIE and CoNi-LDH-NIE. (h) Co K-edge EXAFS spectra for CoNiP-NIE, CoNi-LDH-NIE, Co foil and CoO. (i) Ni K-edge EXAFS spectra for CoNiP-NIE, CoNi-LDH-NIE, Ni foil and NiO.

the carbon cloth [22,23]. Then, the CoNiP-NIE was prepared by *in situ* phosphidation process with CoNi-LDH-NIE as precursor and 0.2 g NaH₂PO₂·H₂O as phosphorus source. Typically, CoNi-LDH-NIE was annealed in N₂ at 300 °C for 1 h, with a heating rate of 5 °C min⁻¹. CoNiP-NIE-x ($x = 0.1, 0.5$ and 1.0) were synthesized with similar method except with 0.1, 0.5 and 1.0 g NaH₂PO₂·H₂O.

In addition, the residual powdery ZIF-67 nanosheet (ZIF-67-P) in solution during the synthesis of ZIF-67 nanoarray was also collected and subsequently treated to obtain CoNi-LDH powders (CoNi-LDH-P) and CoNiP powders (CoNiP-P) sample with the same procedure as that of CoNi-LDH-NIE and CoNiP-NIE respectively.

2.2. Characterization

Scanning electron microscope (SEM) was obtained on Zeiss Supra 55. Elemental mapping was collected by energy-dispersive X-ray spectroscopy (EDS) attached to SEM. High-resolution transmission electron microscope (HRTEM) was obtained on JEOL JEM-2010. X-ray diffraction patterns were carried out by a Shimadzu XRD-6000 diffractometer with Cu K α radiation (scan step: 10° min⁻¹). X-ray photoelectron spectra (XPS) were performed using a Thermo VG ESCALAB 250. The Co and Ni XAFS measurements were performed at the beamline 1W1B of the Beijing Synchrotron Radiation Facility (BSRF), Institute of High Energy Physics (IHEP), Chinese Academy of Sciences (CAS). Extended X-ray absorption fine structure spectra (EXAFS) were recorded at ambient temperature in transmission mode. The typical energy of the storage ring was 2.5 GeV with a maximum current of 250 mA. The Si (111) double crystal monochromator was used. *In situ* Raman spectra were detected by HORIBA Jobin Yvon Raman microspectrometer ($\lambda = 532$ nm). Raman spectra for OER process (1 M KOH) and HMFOR process (1 M KOH+10 mM HMF) at various potentials were collected. The drop contact angles were measured by the optical angle measurement (DSA100) in ambient air at room temperature.

2.3. Electrochemical performance measurements

All electrochemical measurements were performed in a three-electrode system using CHI760E electrochemical workstation (Shanghai Chenhua, China) at room temperature. The nanoarray grown on carbon cloth was directly used as working electrode. Ag/AgCl electrode and Pt wire (graphite rod for HER tests) were used as reference and counter electrode, respectively. The measured potentials vs. Ag/AgCl were converted to a reversible hydrogen electrode (RHE) scale according to the Nernst equation: $E_{\text{RHE}} = E_{\text{Ag/AgCl}} + 0.059 \times \text{pH} + 0.197$.

The powdery samples were coated on carbon cloth with the same loading as nanoarray. The electrocatalysts suspension were prepared by dispersing 4 mg as-synthesized samples in the solution containing of 770 μL DI water, 200 μL ethanol and 30 μL Nafion, and ultrasonication for 30 min. Then, the electrocatalysts suspension were pipetted onto the carbon cloth with a loading 2 mg cm⁻².

The OER and HER were tested in 1 M KOH solution. The HMFOR was conducted in 1 M KOH solution with 10 mM HMF. The linear sweep voltammetry (LSV) with a scan rate of 5 mV s⁻¹ was collected. 95%-iR compensation was applied in all LSV curves. Electrochemical impedance spectroscopy (EIS) measurements were performed in 1 M KOH at 0 V vs. RHE from 10⁻¹ Hz to 10⁵ Hz. The electrochemical surface area (ECSA) was evaluated in terms of the double-layer capacitance (C_{dl}). Cyclic voltammetry (CV) was performed in 1 M KOH at different scan rates of 20, 40, 60, 80, 100 and 120 mV s⁻¹ in non-Faradaic region. The stability of CoNiP-NIE towards HMF oxidation were evaluated by chronoamperometry at 1.5 V vs. RHE in 10 mL 1 M KOH with 10 mM HMF for eight cycles. For the two-electrode electrolyzer, both cathode and anode were CoNiP-NIE or CoNi-LDH-NIE. The stability of CoNiP-NIE two-electrode towards HMFOR were evaluated by chronoamperometry at 1.7 V in 10 mL 1 M KOH with 10 mM HMF for six cycles. The generated H₂ under a two-electrode configuration was quantified

through water drainage method in an H-type electrolytic cell. The *in situ* electrochemical EIS tests were measured over a frequency range from 10⁵ to 10⁻² Hz with AC amplitude of 10 mV without agitation in a three-electrode system.

2.4. Products analysis

The identification and quantification of HMF and oxidation products were conducted by high-performance liquid chromatography (HPLC) on Shimadzu LC-20AT equipped with an ultraviolet-visible ($\lambda = 260$ nm, 280 nm) detector and an Aminex HPX-87 H column (300 mm × 7.8 mm × 9 μm , Bio-Rad). 0.01 M H₂SO₄ solution was employed as chromatographic mobile phase at 60 °C with a rate of 0.80 mL min⁻¹. After ~58 C charges were passed, 20 μL of the electrolyte was withdrawn and diluted with 3980 μL 0.01 M H₂SO₄ solution. The liquid samples were collected after every 10 C of charge at 1.5 V vs. RHE to monitor the change of reactant and products during oxidation process. HMF and oxidation products were quantitatively determined based on the calibration curves of those standard solutions.

The Faradaic efficiency (FE) and yield of oxidation products were calculated by the following equations:

$$\text{Faradaic efficiency}(\%) = \frac{\text{mol of product formed}}{\text{total charge passed}/(F \times n)} \times 100$$

$$\text{Yield}(\%) = \frac{\text{mol of product formed}}{\text{mol of initial HMF}} \times 100$$

where F is the Faraday constant (96,485 C mol⁻¹) and n is the number of electrons required for the oxidation of HMF to products. In detail, 2 electrons are needed for the production of 5-hydroxymethyl-2-furancarboxylic acid (HMFCFA) and 2,5-furandicarboxaldehyde (DFF). 4 and 6 electrons required for the production of 5-formylfuran-2-carboxylic acid (FFCA) and FDCA, respectively.

The FE of H₂ was calculated by the following equations:

$$\text{FE(H}_2\text{)} (\%) = \frac{2N_A \times P \times V_{H_2}/RT}{Q/e} \times 100$$

where N_A is Avogadro's constant (6.022×10^{23}). P stands for the standard atmospheric pressure (101.325 kPa). V_{H_2} (mL) is the volume of H₂ collected by water drainage method. R is the universal gas constant (8.314 J mol⁻¹ K⁻¹). T is the system temperature (298.15 K). e is the amount of charge carried by an electron (1.6×10^{-19} C).

2.5. Solar-driven overall EHCO system

Overall EHCO system was carried out in a two-electrode electrolyzer by CoNiP-NIE and powered by a commercial Si solar cell. The light source employed in tests was a Xe lamp with a standard AM 1.5 G (100 mW cm⁻²). The electrochemical measurements were measured by CHI760E electrochemical workstation without iR compensation.

The solar-to-FDCA conversion efficiency can be calculated:

$$\eta = \frac{E_{eq} \times I_{cell} \times \text{FE}(\%)}{I_{solar} \times A}$$

The solar-to-H₂ conversion efficiency can be calculated:

$$\eta = \frac{1.23 \text{ V} \times I_{cell}}{I_{solar} \times A}$$

where E_{eq} is the thermodynamic equilibrium cell potential of FDCA (0.30 V), I_{cell} is the operating current of the solar cell (67.8 mA), $\text{FE}(\%)$ is the Faradaic efficiency of the FDCA, I_{solar} is 100 mW cm⁻² and A is the surface area of Si solar cell ($4 \times 3.8 \text{ cm}^2$).

2.6. DFT calculation

The density function theory (DFT) calculations were performed using the DMol3 code. The Perdew-Burke-Ernzerhof (PBE) method was used as the exchange-correction function under the scheme of generalized gradient approximation (GGA) [24–27]. Considering the dispersion interactions, the DFT-D correction was employed [28]. A double numerical plus polarization (DNP) basis set was utilized. The convergence tolerance of energy, force and displacement were set to 10^{-5} Hartree, 0.002 Hartree \AA^{-1} and 0.005 \AA , respectively. And a vacuum space of 15 \AA was set to avoid the inter layer interaction. During structural optimizations, a $2 \times 2 \times 1$ k-point mesh as chosen for sampling the Brillouin zone.

3. Results and discussion

3.1. Material characterizations

The hierarchical CoNiP-NIE was prepared as follows: Co-based zeolitic imidazolate frameworks (ZIF-67) with nanoarray structure and smooth surface were firstly synthesized on the carbon cloth (Fig. S1a). Then, ZIF-67 nanoarray was *in-situ* converted into CoNi-LDH nanoarray with wrinkled surface by an ion exchange/etching method (Fig. S1b). Last, the CoNiP-NIE with the maintained nanoarray structure was obtained via a phosphidation strategy (Fig. 1b). The whole preparation process is simple and controllable, which can be effectively realized the large-scale preparation with an area of 496 cm^2 ($31 \text{ cm} \times 16 \text{ cm}$) and a homogeneous surface morphology (Fig. S2). The CoNiP nanosheet with width of $\sim 900 \text{ nm}$ (the widest place) and thickness of $\sim 70 \text{ nm}$ was revealed by scanning electron microscopy (SEM, Fig. 1b). Transition electron microscopy (TEM) image shows that lots of nanoparticles disperse uniformly on the surface of CoNiP nanoarray (Fig. 1c). The lattice fringe with a spacing of 0.22 nm is ascribed to the (111) plane of CoNiP (Fig. 1c) [29]. Moreover, relative energy dispersive X-ray spectrometry (EDS) elemental mapping shows a well-uniformed distribution of Co, Ni, P and C in CoNiP-NIE (Fig. S3).

As can be seen from X-ray diffraction (XRD) patterns (Fig. 1d), ZIF-67 is fully transformed into CoNi-LDH after ion exchange/etching process, from which the peaks of ZIF-67 are vanished and two peaks at $\sim 11.6^\circ$ and 34.9° are appeared, attributing to the (003) and (012) planes of LDHs (PDF#40-0215) [9]. After phosphidation treatment, the reflections located at $\sim 30.6^\circ$, 41.0° and 54.7° are corresponding to (110), (111) and (002) planes of CoNiP (PDF#71-2336), confirming the phase transformation from hydroxide to phosphide. Furthermore, X-ray photoelectron spectroscopy (XPS) was conducted to analyze the element composition and valence state, which reveals the presence of Co, Ni and P elements in CoNiP-NIE (Fig. S4 and Table S1). Both Co and Ni in CoNi-LDH-NIE are confirmed by high-resolution Co 2p and Ni 2p spectra to be oxidation state (Fig. 1e and f) [30,31]. However, an obviously negative shift for both Co and Ni signals could be observed after phosphidation treatment, indicating the reduced valence state. Two pairs of new peaks appeared at $\sim 778.3/793.4 \text{ eV}$ and $853.1/870.4 \text{ eV}$ are endorsed to $\text{Co}^{\delta+}\text{-P}$ and $\text{Ni}^{\delta+}\text{-P}$, respectively (Fig. 1e and f) [32,33]. In the high-resolution P 2p spectrum (Fig. 1g), the peaks at ~ 129.3 and 130.3 eV are assigned to $\text{P } 2\text{p}_{3/2}$ and $2\text{p}_{1/2}$ of P in the form of metal phosphide, further demonstrating the successful formation of CoNiP. In addition, the peak at $\sim 133.5 \text{ eV}$ can be ascribed to PO_4^{3-} or P_2O_5 , resulting from the exposure of the product to air [34,35].

X-ray absorption near-edge structure (XANES) spectra were further performed to investigate electronic structure information, and Fourier transform of Co and Ni K-edge extended X-ray adsorption fine structure (EXAFS) oscillations were used to illustrate the detailed atomic configuration. The position of white line for CoNiP-NIE in Co K-edge XANES is located between Co foil and CoO reference, suggesting that the valence state of Co in CoNiP-NIE situated between 0 and +2 (Fig. S5a). The corresponding EXAFS spectrum of CoNiP-NIE shows two peaks at 1.64

and 2.24 \AA , attributing to the Co-P and Co-Co coordination, respectively, which are derived from Co-O (1.33 \AA) and Co-Co (2.71 \AA) coordination of CoNi-LDH-NIE after phosphidation treatment (Fig. 1h) [17]. A similar situation is also observed for Ni in CoNiP-NIE revealed by Ni K-edge XANES and corresponding EXAFS spectrum, which are also consistent with XPS results (Figs. S5b and 1i) [9]. The above results proved that CoNiP-NIE was successfully obtained from CoNi-LDH-NIE through phosphidation treatment.

3.2. Electrochemical performance

The electrocatalytic performance of CoNiP-NIE for HMFOR were evaluated in 1 M KOH with 10 mM HMF (Fig. 2a). Remarkably, CoNiP-NIE presents an ultralow potential of 1.29 V vs. RHE for HMFOR at a current density of 20 mA cm^{-2} (denoted as j_{20}), which is much lower than that for OER (1.58 V vs. RHE , tested in 1 M KOH). Moreover, the current density at 1.50 V vs. RHE (denoted as $j_{1.5}$) also increased from 5.39 to 58.25 mA cm^{-2} , further indicating a superior activity for HMFOR. Compared to CoNiP-NIE, CoNi-LDH-NIE exhibits inferior HMFOR performance in terms of higher potential ($\eta_{20} = 1.38 \text{ V vs. RHE}$) and lower current density ($j_{1.5} = 26.75 \text{ mA cm}^{-2}$). In addition, the small oxidation peaks of LSV curves before 1.4 V vs. RHE are due to the oxidation of Co^{2+} and Ni^{2+} [36]. High-performance liquid chromatography (HPLC) was used to identify the oxidation products and quantify the corresponding FE and yield. A total charge of $\sim 58 \text{ C}$ is passed under various potentials during HMFOR process, which is the same as the theoretical value, indicating that HMF is completely consumed. Both FDCA, 5-hydroxymethyl-2-furancarboxylic acid (HMFC), 5-formylfuran-2-carboxylic acid (FFCA) and 2,5-furandicarboxaldehyde (DFF) were detected during overall electrocatalytic process for CoNiP-NIE and CoNi-LDH-NIE, but FDCA was the final product (Fig. S6). The FE_{FDCA} and yield of FDCA for CoNiP-NIE and CoNi-LDH-NIE are similar at low potentials (below 1.60 V vs. RHE). However, when the applied potential exceeding 1.60 V vs. RHE , the FE_{FDCA} and yield for CoNi-LDH-NIE decrease sharply to less than 69.6% and 68.4% at 1.70 V vs. RHE . Surprisingly, the FE_{FDCA} and yield for CoNiP-NIE remain at 81.9% and 85.8% even under 1.70 V vs. RHE (the maximum FE_{FDCA} is 87.2% at 1.50 V vs. RHE), showing a wider catalytic potential range for HMFOR than CoNi-LDH-NIE and other reported works at high potentials (Fig. 2b-c) [16,17,19,36,37], which is conducive to the rapid generation of FDCA under high current. Eight successive cycles at 1.50 V vs. RHE were tested to evaluate the durability of CoNiP-NIE for HMFOR (Fig. 2d), showing a remarkable cycle stability with almost unchangeable FE_{FDCA} and yield.

Subsequently, the HER performance of CoNiP-NIE were also investigated in 1 M KOH to assess its bifunctional ability. Remarkably, CoNiP-NIE exhibits superior HER activity with the lower overpotential of 107.56 and 190.76 mV to drive a current density of -10 and -100 mA cm^{-2} compared with CoNi-LDH-NIE (278.44 and 363.13 mV), respectively (Fig. 2e and f). The lower Tafel slope ($74.36 \text{ mV dec}^{-1}$) than CoNi-LDH-NIE ($78.13 \text{ mV dec}^{-1}$) indicates a faster HER kinetics (Fig. S7). Moreover, electrochemical impedance spectra (EIS) show that CoNiP-NIE possesses a much smaller charge transfer resistance ($R_{\text{ct}} = \sim 2.60 \Omega$) than CoNi-LDH-NIE ($R_{\text{ct}} = \sim 3.57 \Omega$), indicating a better electron transport ability (Fig. S8).

The lower overpotential, smaller Tafel slope and better conductivity of CoNiP-NIE than CoNi-LDH indicate the positive effect of phosphidation treatment toward HER activity. The influences of phosphating degree on activity for HMFOR and HER were further explored. During phosphidation process, different dosage of $\text{NaH}_2\text{PO}_2 \cdot \text{H}_2\text{O}$ ($0.1, 0.2, 0.5$ and 1.0 g) were adopted and the obtained samples were denoted as CoNiP-NIE-x ($x = 0.1, 0.2, 0.5$ and 1.0). All CoNiP-NIE samples present similar array structure while the thickness of nanosheet gradually increases with increasing phosphorus precursor (Fig. S9). The diffraction peaks of CoNiP are also observed in all CoNiP-NIE samples, but some PO_x signals locate between 10° and 35° appeared in CoNiP-NIE-0.5 and

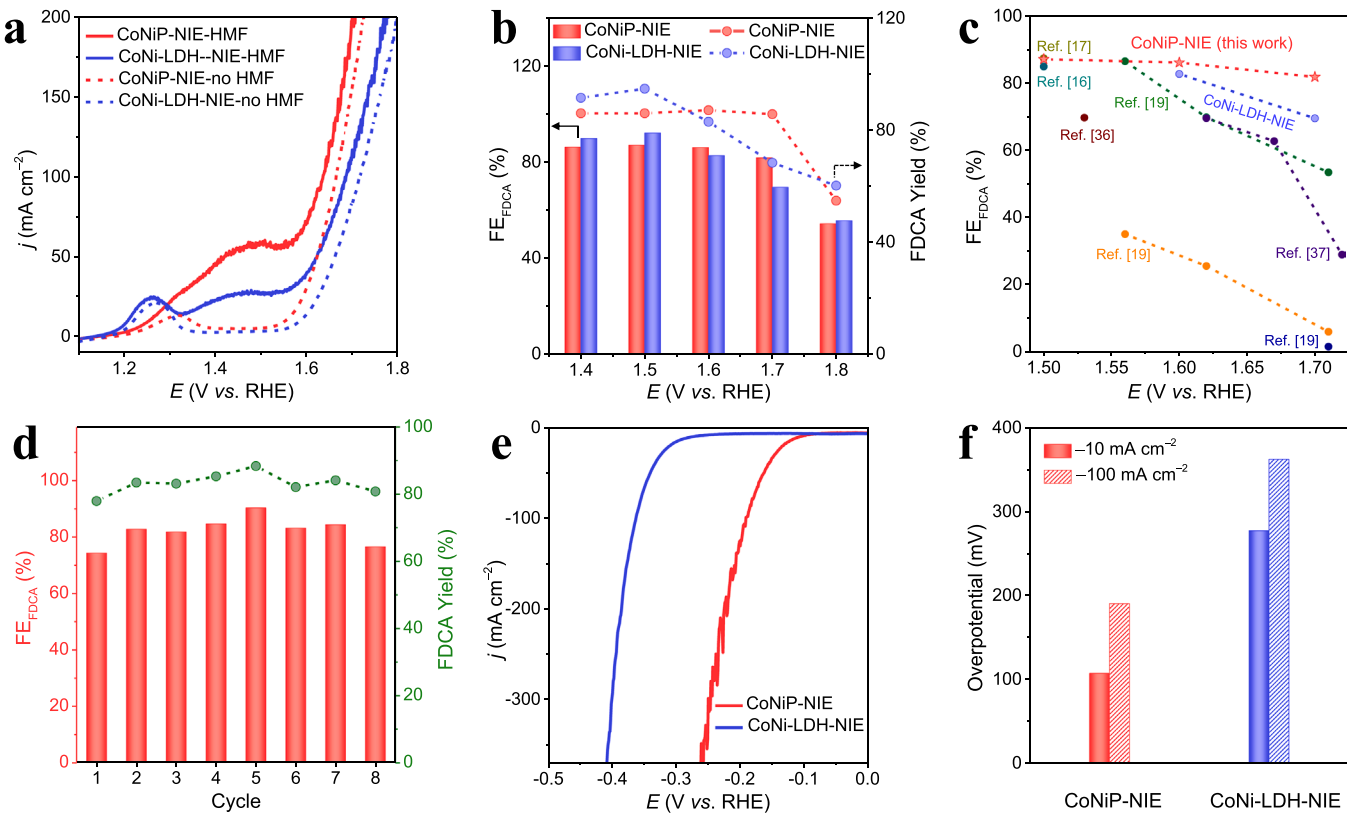


Fig. 2. (a) LSV curves of CoNiP-NIE and CoNi-LDH-NIE in 1 M KOH in the presence and absence of 10 mM HMF. (b) FE_{FDCA} and yield of CoNiP-NIE and CoNi-LDH-NIE at different potentials. (c) Comparison of the HMFOR performance of this work against previously reported transition metal catalysts at high potentials. (d) Eight successive cycles at 1.50 V vs. RHE of CoNiP-NIE during HMFOR. (e) LSV curves and (f) overpotentials at -10 and -100 mA cm^{-2} of CoNiP-NIE and CoNi-LDH-NIE in 1 M KOH for HER.

CoNiP-NIE-1.0, might be caused by inevitable oxidation process when exposed in air (Fig. S10). Structure-activity relationships were deduced revealing a volcano-type behavior for the electrocatalytic activity and the phosphating degree. CoNiP-NIE-0.2 produced the highest FE_{FDCA} and yield for HMFOR, and lower overpotential and faster reaction kinetics for HER compared to other CoNiP samples (Fig. S11 and S12). It was speculated that the electrical conductivity of CoNiP-NIE was improved by a moderate amount of phosphorus, but excessive phosphorus would form thick layer of PO_x , which could hinder the contact between active site and reactants and reduced the catalytic performance.

The used CoNiP-NIE after HMFOR and HER tests was characterized in detail by SEM, XRD and XPS. Typically, the nanoarray structure of CoNiP-NIE maintains well after HMFOR and HER tests (Fig. S13). The crystal structure of CoNiP-NIE also maintains well with clear diffraction peaks after HMFOR tests (Fig. S14a), while some diffraction peaks of $M(\text{OH})_2$ ($M = \text{Co}$ or Ni) appear after HER tests (PDF#30-0443, PDF#14-0117) [38]. It is speculated that the local alkalinity is increased during HER process, and metal ions combine with OH^- to form $M(\text{OH})_2$ ($M = \text{Co}$ or Ni). XPS results show that the signal peaks of Co-P and Ni-P disappear after both cases in the high-resolution Co 2p (Fig. S14b) and Ni 2p spectra (Fig. S14c). However, in the high-resolution P 2p spectrum, there is still a weak Co-Ni-P diffraction peak after HER (Fig. S14d) [32,34].

The reduced overpotential in cathodic reaction on CoNiP-NIE and in anodic reaction after replacing OER with HMFOR could play an important role in improving the efficiency of hydrogen production. A novel EHCO system for HMFOR and HER was constructed based on CoNiP-NIE (CoNiP/HMFOR&HER), which exhibits excellent performance with only 1.46 V to reach a current density of 20 mA cm^{-2} , significantly superior to CoNi-LDH/HMFOR&HER (1.79 V) and CoNiP/

OER&HER (1.76 V, Fig. 3a). The FE_{FDCA} and yield for CoNiP/HMFOR&HER (80.8% and 82.6% at 1.70 V) are much higher than that for CoNi-LDH/HMFOR&HER (41.8% and 40.9% at 1.70 V) under various potentials, and the difference was more obvious at the high potentials (Fig. 3b). In addition, it was found that CoNiP-NIE took much less time than CoNi-LDH-NIE to reach the same quantity of electric charge during test, indicating a fast reaction rate. Compared with traditional water splitting system ($16.1 \text{ L h}^{-1} \text{ m}^{-2}$), the evolution rate of H_2 in this proposed novel EHCO system is significantly accelerated owing to enhanced reaction efficiency ($41.2 \text{ L h}^{-1} \text{ m}^{-2}$, Fig. 3c and S15), which is ~ 2.6 times of water splitting system. Besides, the solid FDCA product was collected by acidizing electrolyte after HMFOR ($85.5 \text{ g h}^{-1} \text{ m}^{-2}$) (Fig. 3c). The light-yellow powders were further confirmed by HPLC and ^1H NMR to be FDCA without any other impurities, showing promising feasibility for preparation and collection of FDCA (Fig. 3c and S16). Moreover, the system could work solidly for six cycles at high voltage (1.70 V) without performance degradation (Fig. S17). The electrochemical method powered by clean energy is one of the important ways to gain high-purity hydrogen in the future [39]. As a step further, a commercial Si solar cell with an open-circuit voltage of 2.38 V and a short-circuit current of 113.1 mA was employed to drive the EHCO system (Fig. 3d and S18a-b). The working voltage and current can be derived from the intersection point between the I - V curve of solar cell and the LSV of EHCO system, which are determined to be 2.16 V and 67.8 mA, respectively (Fig. 3d). During the reaction progress, the actual working current decreases from 58.8 to 23.5 mA due to the gradual consumption of HMF (Fig. S18c). The FE_{FDCA} and overall solar-to-FDCA conversion efficiency in this period are analyzed to be 58.6% and 0.8%, and the solar-to- H_2 conversion efficiency is 5.5%, which opens the way for clean energy like solar to power EHCO systems. These results unambiguously prove that CoNiP-NIE is competent for both HMFOR and

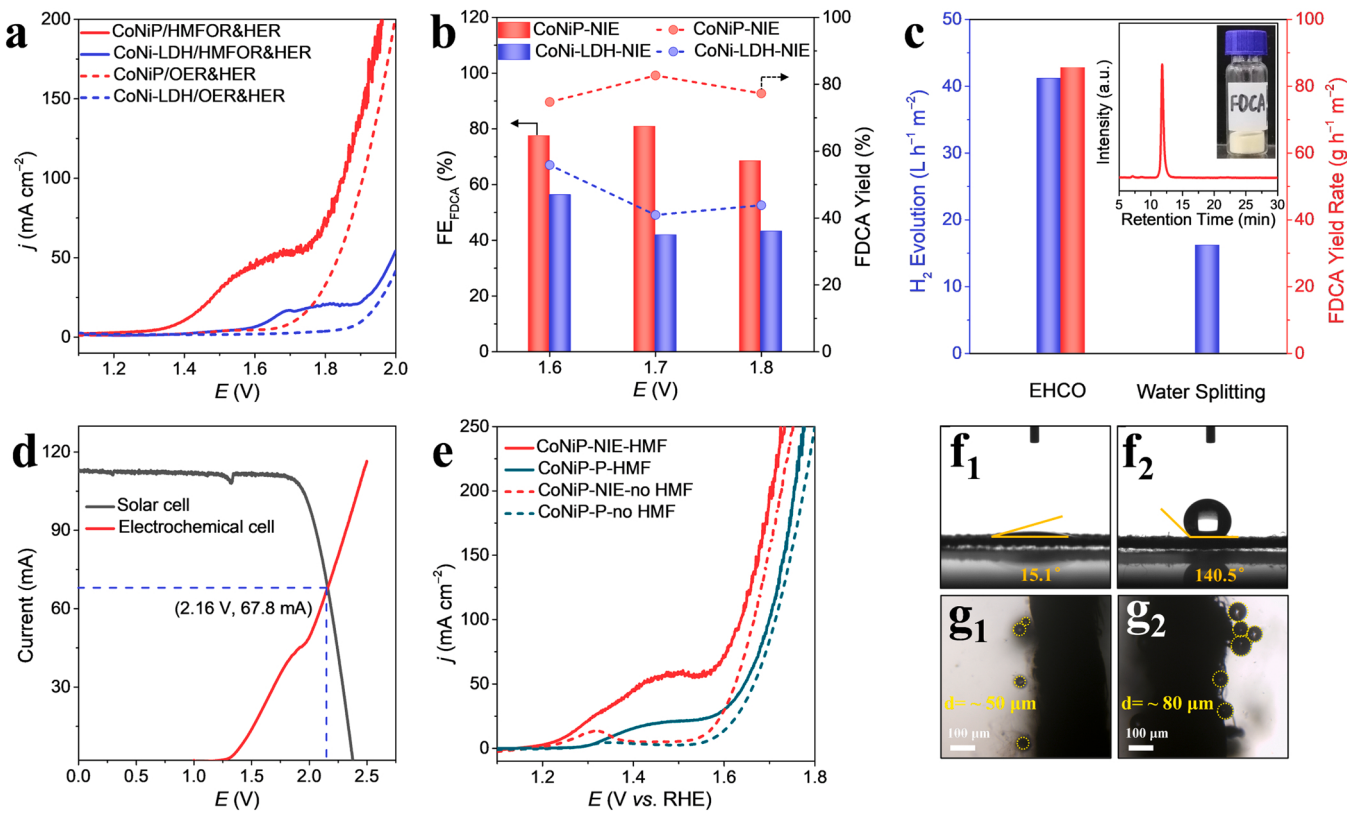


Fig. 3. (a) LSV curves of CoNiP-NIE and CoNi-LDH-NIE for EHCO and water splitting, (b) FE_{FDCA} and yield at different potentials of CoNiP-NIE and CoNi-LDH-NIE for EHCO. (c) H_2 evolution rate and FDCA yield rate of CoNiP-NIE for EHCO system and water splitting system (the inset shows HPLC chromatogram and digital photograph of FDCA powders). (d) I - V curve of commercial Si solar cell under illumination together with polarization curve of the catalytic cell. (e) LSV curves of CoNiP-NIE and CoNiP-P in 1 M KOH in the presence and absence of 10 mM HMF. The connect angles of (f₁) CoNiP-NIE and (f₂) CoNiP-P. Microscope photographs of H_2 bubbles on the surface of (g₁) CoNiP-NIE and (g₂) CoNiP-P.

HER, and coupling these two reactions is more thermodynamically and kinetically favorable than traditional water splitting for hydrogen production.

To demonstrate the merits of the nanoarray integrated electrode, CoNiP powder sample (CoNiP-P) was synthesized with the same element composition as CoNiP-NIE and coated on carbon substrate with same mass-loading (Fig. S19 and S20). Remarkably, CoNiP-NIE shows much improved electrocatalytic activity for HMFOR with a potential of 1.29 V vs. RHE at 20 mA cm^{-2} than CoNiP-P counterpart (1.46 V vs. RHE) (Fig. 3e). In addition, the FE_{FDCA} and yield for CoNiP-P is only 66.6% and 60.5% at 1.60 V vs. RHE, respectively, obviously less than that for CoNiP-NIE (86.2% and 87.2%), demonstrating an enhanced efficiency due to the hierarchical nanoarray structure (Fig. S21). Moreover, CoNiP-NIE displays larger electrochemical surface area of 12.98 mF cm^{-2} and smaller resistance ($R_s = \sim 2.82 \Omega$, $R_{ct} = \sim 2.60 \Omega$) than CoNiP-P (4.68 mF cm^{-2} , $R_s = \sim 5.15 \Omega$, $R_{ct} = \sim 3.18 \Omega$) (Fig. S22a-d). Due to hierarchical structure of nanoarray integrated electrode, CoNiP-NIE performs much more hydrophilic surface with a contact angle of 15.1° than CoNiP-P (140.5°, hydrophobic state), which is beneficial for mass diffusion and surface reaction process (Fig. 3 f₁-f₂) [21]. *In-situ* optical microscope was also conducted to monitor the surface condition during reaction. With increasing reaction time, the hydrogen bubbles with a diameter of less than 50 μm generate on the surface of CoNiP-NIE, and desorb and release into electrolyte rapidly, demonstrating a smooth gas diffusion process (Fig. 3 g₁ and Video S1). In contrast, the bubbles agglomerate rapidly on the surface of CoNiP-P, which will inevitably cover the active site (Fig. 3 g₂ and Video S2). The above results indicate that constructing integrated electrode is beneficial to the mass diffusion and electron transfer process, and thus enhances the performance of HMFOR and HER.

3.3. Mechanism discussion

The reaction pathways and reaction mechanism of CoNiP-NIE for HMFOR were further explored through *in-situ* techniques. It has been reported that there are two pathways for HMFOR, one is that DFF pathway through alcohol oxidation and the other is that HMFCA pathway through aldehyde oxidation (Fig. S23) [40]. The results show that HMF was gradually consumed while FDCA was gradually generated with the increasing of charge on CoNiP-NIE (Fig. 4a and b). Moreover, HMFCA and FFCA were also detected, and the concentration of HMFCA increased first and then decreased, indicating that it was consumed as a key intermediate during the reaction process. However, DFF was almost undetectable during overall process, demonstrating HMFOR is followed the HMFCA pathway, that is, the aldehyde group of HMF is first oxidized to carboxyl group.

In addition, the *in-situ* potential-dependent Raman spectra were carried out to investigate the reaction mechanism of HMFOR over CoNiP-NIE. For both HMFOR and OER process, no obvious signals could be detected when the applied potential below 1.52 V vs. RHE. When the applied potential reaching to 1.52 V vs. RHE, two peaks appeared at 465 and 550 cm^{-1} for OER process, which are attributed to Ni-O vibrations of NiOOH, and their intensity increased gradually with increasing applied potentials (Fig. 4c) [41]. Notably, the signals of Ni-O vibrations weakened or even disappeared when the applied potential returning to 1.72 V vs. RHE, probably due to the large number of bubbles generated violently during the OER process without HMF. After adding HMF, the signals of Ni-O vibrations are delayed until the applied potential reaching to 1.62 V vs. RHE (Fig. 4d), indicating the oxidation of HMF may be accompanied by the reduction of Ni^{III} in NiOOH to Ni^{II}, thus the signals of NiOOH cannot be detected under lower potential. When

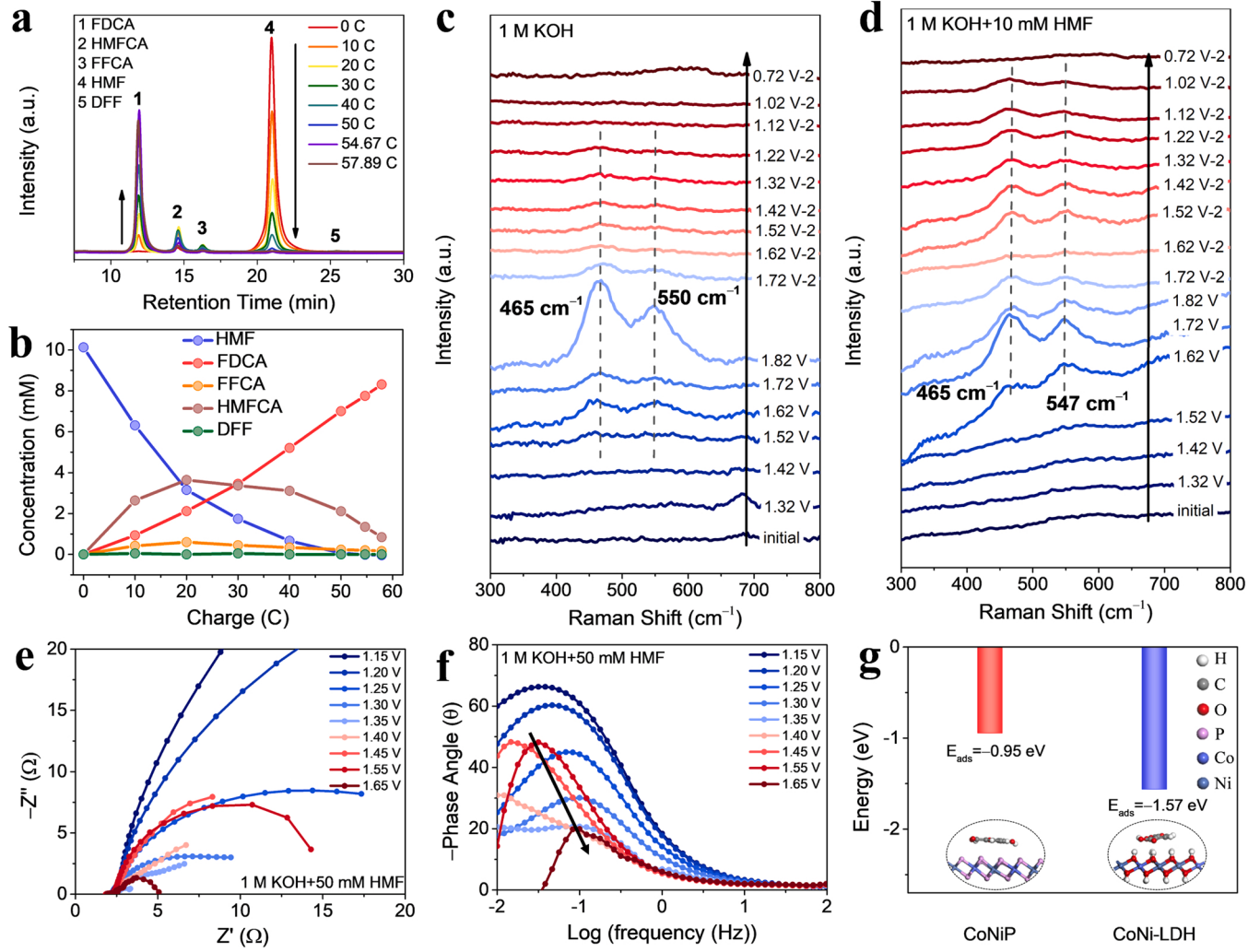


Fig. 4. (a) HPLC chromatogram traces and (b) concentration of HMF and oxidation products with increasing charge during the HMFOR catalyzed by CoNiP-NIE at 1.50 V vs. RHE. *In-situ* Raman spectra (c) in 1 M KOH and (d) 1 M KOH+ 10 mM HMF at different potentials. (e) *In-situ* Nyquist plots and (f) Bode phase plots of CoNiP-NIE at various potentials in 1 M KOH with 50 mM HMF. (g) Absorption energy of FDCA on the surfaces of CoNiP and CoNi-LDH.

applied potential exceeding 1.62 V vs. RHE, OER starts and generates much oxygen-containing intermediate species, promoting the formation of NiOOH. In addition, the peaks are recovered when the potential is back to more negative potential, indicating that the CoNiP-NIE features a reversible structure evolution and recovery [41].

The *in-situ* potential-dependent EIS measurements are performed to further investigate the catalytic kinetics of CoNiP-NIE. At the low potential of 1.15 ~ 1.20 V vs. RHE, the Nyquist plots of CoNiP-NIE for HMFOR show approximated vertical lines, which indicate high charge transfer resistance. When the potential increases to 1.25 V vs. RHE, there is a significant change and a semicircle begins to take shape, which indicates the beginning of the Faradaic reaction (Fig. 4e) [42]. It marks the beginning of HMFOR at this potential, which is consistent with LSV results (Fig. 2a). However, the Nyquist plots of CoNiP-NIE for OER are a steep line before 1.55 V vs. RHE, and appear a significant semicircle until 1.55 V vs. RHE, suggesting that OER occurs relatively lagging (Fig. S24a). The corresponding Bode phase plots of CoNiP-NIE for HMFOR and OER present two electrochemical processes, which are associated with interface reaction charge transfer in the low frequency region and surface oxidation interface in the high frequency region, respectively [43]. Compared with HMFOR process, the peak shifts to lower phase angle and higher frequency in OER process after 1.55 V vs. RHE, mainly attributing to the accelerating of surface metal oxidation kinetics, which indicates that the oxidized surface can be partially

reduced by HMF (Fig. 4f and S24b).

To further reveal the structure-activity relationship for CoNiP, density functional theory (DFT) calculations were performed with CoNiP and CoNi-LDH as models (Fig. S25 and S26). The total density of states (TDOS) of CoNiP and CoNi-LDH are displayed in Fig. S27a. CoNiP shows a higher density of states surrounding Femi level, indicating an improved electrical conductivity [44], which is consistent with EIS result (Fig. S8). Although the adsorption energy of HMF on CoNiP (-1.02 eV) is slightly lower than that on CoNiP (-1.20 eV), the adsorption energy of FDCA on CoNiP (-0.95 eV) is much lower than that on CoNi-LDH (-1.57 eV), suggesting the generated FDCA is more easily desorbed from CoNiP surface (Fig. 4g and S27b). Especially at the high potential, the rapid release of the product provides reaction sites for subsequent reactions, which is important for the whole reaction progress. This indicates that CoNiP effectively enhances the electrical conductivity of electrode and facilitates desorption of FDCA molecule from electrode surface.

4. Conclusion

In summary, we demonstrated a bifunctional CoNiP-NIE with boosted performance of HMFOR and HER simultaneously. The FE_{FDCA} on CoNiP-NIE can reach to 87.2% at 1.50 V vs. RHE and remain stable (more than 82%) in a wide potential from 1.40 V to 1.70 V vs. RHE for

HMFOR. Moreover, CoNiP-NIE also shows superior HER activity with a low overpotential of 107.56 mV to deliver -10 mA cm^{-2} . Furthermore, the EHCO system based on bifunctional CoNiP-NIE exhibits an ultra-lower cell potential (1.46 V) and higher evolution rate of H_2 ($41.2 \text{ L h}^{-1} \text{ m}^{-2}$), outperforms that of water splitting system (1.76 V, $16.1 \text{ L h}^{-1} \text{ m}^{-2}$). A high FDCA yield rate ($85.5 \text{ g h}^{-1} \text{ m}^{-2}$) can be achieved on this ECHO system, further increase the economic efficiency for hydrogen production. *In-situ* EIS and Raman spectra demonstrate that CoNiP undergoes the surface metal oxidation and a subsequent partial reduction by HMF. Theoretical calculations indicate that CoNiP shows an enhanced electrical conductivity and moderate desorption for FDCA, which endow it superior catalytic performance. This work thus could provide a successful paradigm for rational design bifunctional electrocatalysts for highly efficient hydrogen production coupled with biomass oxidation.

Credit author statement

Mingfei Shao and Wenfu Xie conceived and supervised the project. **Yuke Song** conducted material synthesis, carried out the catalytic performance test and wrote the paper. **Yingjie Song, Shijin Li and Shan Jiang** assisted with the experiments. **Hao Li and Jin Yong Lee** conducted the theoretical calculations. The manuscript was primarily written by **Yuke Song, Mingfei Shao and Wenfu Xie** revised. All authors contributed to discussions and manuscript reviews.

Declaration of Competing Interest

The authors declare that they have no known competing financial interests or personal relationships that could have appeared to influence the work reported in this paper.

Acknowledgments

This work was supported by the National Natural Science Foundation of China (22109004, 22090031, 21922501), Project funded by China Postdoctoral Science Foundation (2021M690319). The authors thank the BL1W1B in the Beijing Synchrotron Radiation Facility (BSRF).

Appendix A. Supporting information

Supplementary data associated with this article can be found in the online version at [doi:10.1016/j.apcatb.2022.121400](https://doi.org/10.1016/j.apcatb.2022.121400).

References

- [1] J. Joo, T. Kim, J. Lee, S.-I. Choi, K. Lee, Morphology-controlled metal sulfides and phosphides for electrochemical water splitting, *Adv. Mater.* 31 (2019) 1806682.
- [2] Z.W. Seh, J. Kibsgaard, C.F. Dickens, I. Chorkendorff, J.K. Norskov, T.F. Jaramillo, Combining theory and experiment in electrocatalysis: insights into materials design, *Science* 355 (2017) eaad4998.
- [3] L. Zhou, M.F. Shao, J.B. Li, S. Jiang, M. Wei, X. Duan, Two-dimensional ultrathin arrays of CoP: electronic modulation toward high performance overall water splitting, *Nano Energy* 41 (2017) 583–590.
- [4] S.A. Akhade, N. Singh, O.Y. Gutierrez, J. Lopez Ruiz, H. Wang, J.D. Holladay, Y. Liu, A. Karkamkar, R.S. Weber, A.B. Padmaperuma, M.S. Lee, G.A. Whyatt, M. Elliott, J.E. Holladay, J.L. Male, J.A. Lercher, R. Rousseau, V.A. Glezakou, Electrocatalytic hydrogenation of biomass-derived organics: a review, *Chem. Rev.* 120 (2020) 11370–11419.
- [5] Y. Li, X. Wei, L. Chen, J. Shi, Electrocatalytic hydrogen production trilogy, *Angew. Chem. Int. Ed.* 60 (2021) 19550–19571.
- [6] Y. Song, K. Ji, H. Duan, M. Shao, Hydrogen production coupled with water and organic oxidation based on layered double hydroxides, *Exploration* 1 (2021) 20210050.
- [7] K. Xiang, D. Wu, X. Deng, M. Li, S. Chen, P. Hao, X. Guo, J.L. Luo, X.Z. Fu, Boosting H_2 generation coupled with selective oxidation of methanol into value-added chemical over cobalt hydroxide@hydroxysulfide nanosheets electrocatalysts, *Adv. Funct. Mater.* 30 (2020) 1909610.
- [8] Y.X. Chen, A. Lavacchi, H.A. Miller, M. Bevilacqua, J. Filippi, M. Innocenti, A. Marchionni, W. Oberhauser, L. Wang, F. Vizza, Nanotechnology makes biomass electrolysis more energy efficient than water electrolysis, *Nat. Commun.* 5 (2014) 4036.
- [9] L. Zhou, M.F. Shao, C. Zhang, J. Zhao, S. He, D. Rao, M. Wei, D.G. Evans, X. Duan, Hierarchical CoNi-sulfide nanosheet arrays derived from layered double hydroxides toward efficient hydrazine electrooxidation, *Adv. Mater.* 29 (2017) 1604080–1604087.
- [10] C. Wang, H. Lu, Z. Mao, C. Yan, G. Shen, X. Wang, Bimetal schottky heterojunction boosting energy-saving hydrogen production from alkaline water via urea electrocatalysis, *Adv. Funct. Mater.* 30 (2020) 2000556.
- [11] B. You, X. Liu, N. Jiang, Y. Sun, A general strategy for decoupled hydrogen production from water splitting by integrating oxidative biomass valorization, *J. Am. Chem. Soc.* 138 (2016) 13639–13646.
- [12] Y. Yang, T. Mu, Electrochemical oxidation of biomass derived 5-hydroxymethylfurfural (HMF): pathway, mechanism, catalysts and coupling reactions, *Green Chem.* 23 (2021) 4228–4254.
- [13] D.A. Giannakoudakis, J.C. Colmenares, D. Tsiplikides, K.S. Triantafyllidis, Nanoengineered electrodes for biomass-derived 5-hydroxymethylfurfural electrocatalytic oxidation to 2,5-furandicarboxylic acid, *ACS Sustain. Chem. Eng.* 9 (2021) 1970–1993.
- [14] Z. Zhang, K. Deng, Recent advances in the catalytic synthesis of 2,5-furandicarboxylic acid and its derivatives, *ACS Catal.* 5 (2015) 6529–6544.
- [15] M. Park, M. Gu, B.S. Kim, Tailorable electrocatalytic 5-hydroxymethylfurfural oxidation and H_2 production: architecture-performance relationship in bifunctional multilayer electrodes, *ACS Nano* 14 (2020) 6812–6822.
- [16] M.J. Kang, H. Park, J. Jegal, S.Y. Hwang, Y.S. Kang, H.G. Cha, Electrocatalysis of 5-hydroxymethylfurfural on cobalt based spinel catalysts with filamentous nanoarchitecture in alkaline media, *Appl. Catal. B Environ.* 242 (2019) 85–91.
- [17] Y. Song, Z. Li, K. Fan, Z. Ren, W. Xie, Y. Yang, M. Shao, M. Wei, Ultrathin layered double hydroxides nanosheets array towards efficient electrooxidation of 5-hydroxymethylfurfural coupled with hydrogen generation, *Appl. Catal. B Environ.* 299 (2021), 120669.
- [18] B. You, N. Jiang, X. Liu, Y. Sun, Simultaneous H_2 generation and biomass upgrading in water by an efficient noble-metal-free bifunctional electrocatalyst, *Angew. Chem. Int. Ed.* 55 (2016) 9913–9917.
- [19] M. Zhang, Y. Liu, B. Liu, Z. Chen, H. Xu, K. Yan, Trimetallic NiCoFe-layered double hydroxides nanosheets efficient for oxygen evolution and highly selective oxidation of biomass-derived 5-hydroxymethylfurfural, *ACS Catal.* 10 (2020) 5179–5189.
- [20] W.J. Liu, L. Dang, Z. Xu, H.Q. Yu, S. Jin, G.W. Huber, Electrochemical oxidation of 5-hydroxymethylfurfural with NiFe layered double hydroxide (LDH) nanosheet catalysts, *ACS Catal.* 8 (2018) 5533–5541.
- [21] Y. Song, W. Xie, M. Shao, Recent advances in integrated electrode for electrocatalytic carbon dioxide reduction, *Acta Phys. Chim. Sin.* 38 (2022) 2101028.
- [22] Y. Song, W. Xie, S. Li, J. Guo, M. Shao, Hierarchical hollow Co/N-C@Ni₂O₄ microsphere as an efficient bi-functional electrocatalyst for rechargeable Zn-air battery, *Front. Mater.* 6 (2019) 261.
- [23] C. Guan, X. Liu, W. Ren, X. Li, C. Cheng, J. Wang, Rational design of metal-organic framework derived hollow Ni₂O₄ arrays for flexible supercapacitor and electrocatalysis, *Adv. Energy Mater.* 7 (2017) 1602391–1602398.
- [24] G. Kresse, J. Furthmüller, Efficient iterative schemes for ab initio total-energy calculations using a plane-wave basis set, *Phys. Rev. B* 54 (1996) 11169–11186.
- [25] G. Kresse, D. Joubert, From ultrasoft pseudopotentials to the projector augmented-wave method, *Phys. Rev. B* 59 (1999) 1758–1775.
- [26] J.P. Perdew, J.A. Chevary, S.H. Vosko, K.A. Jackson, M.R. Pederson, D.J. Singh, C. Fiolhais, Atoms, molecules, solids, and surfaces: applications of the generalized gradient approximation for exchange and correlation, *Phys. Rev. B* 46 (1992) 6671–6687.
- [27] J.P. Perdew, Y. Wang, Accurate and simple analytic representation of the electron-gas correlation energy, *Phys. Rev. B* 45 (1992) 13244–13249.
- [28] S. Grimme, J. Antony, S. Ehrlich, H. Krieg, A consistent and accurate ab initio parametrization of density functional dispersion correction (DFT-D) for the 94 elements H-Pu, *J. Chem. Phys.* 132 (2010), 154104.
- [29] S. Surendran, S. Shanmugapriya, A. Sivanantham, S. Shanmugam, R. Kalai Selvan, Electrospun carbon nanofibers encapsulated with NiCoP: a multifunctional electrode for supercapattery and oxygen reduction, oxygen evolution, and hydrogen evolution reactions, *Adv. Energy Mater.* 8 (2018) 1800555.
- [30] W. Wang, Y. Lu, M. Zhao, R. Luo, Y. Yang, T. Peng, H. Yan, X. Liu, Y. Luo, Controllable tuning of cobalt nickel-layered double hydroxide arrays as multifunctional electrodes for flexible supercapattery device and oxygen evolution reaction, *ACS Nano* 13 (2019) 12206–12218.
- [31] M.U. Tahir, H. Arshad, W. Xie, X. Wang, M. Nawaz, C. Yang, X. Su, Synthesis of morphology controlled Ni-Co-LDH microflowers derived from ZIF-67 using binary additives and their excellent asymmetric supercapacitor properties, *Appl. Surf. Sci.* 529 (2020), 147073.
- [32] C. Du, L. Yang, F. Yang, G. Cheng, W. Luo, Nest-like NiCoP for highly efficient overall water splitting, *ACS Catal.* 7 (2017) 4131–4137.
- [33] L. He, L. Gong, M. Gao, C.W. Yang, G.P. Sheng, In situ formation of NiCoP@phosphate nanocages as an efficient bifunctional electrocatalyst for overall water splitting, *Electrochim. Acta* 337 (2020), 135799.
- [34] E. Hu, Y. Feng, J. Nai, D. Zhao, Y. Hu, X.W. Lou, Construction of hierarchical Ni-Co-P hollow nanobricks with oriented nanosheets for efficient overall water splitting, *Energy Environ. Sci.* 11 (2018) 872–880.
- [35] R. Zhang, J. Huang, G. Chen, W. Chen, C. Song, C. Li, K. Ostrikov, In situ engineering bi-metallic phospho-nitride bi-functional electrocatalysts for overall water splitting, *Appl. Catal. B Environ.* 254 (2019) 414–423.

- [36] B.J. Taitt, D.H. Nam, K.S. Choi, A comparative study of nickel, cobalt, and iron oxyhydroxide anodes for the electrochemical oxidation of 5-hydroxymethylfurfural to 2,5-furandicarboxylic acid, *ACS Catal.* 9 (2018) 660–670.
- [37] X. Huang, J. Song, M. Hua, Z. Xie, S. Liu, T. Wu, G. Yang, B. Han, Enhancing the electrocatalytic activity of CoO for the oxidation of 5-hydroxymethylfurfural by introducing oxygen vacancies, *Green Chem.* 22 (2020) 843–849.
- [38] H. Sun, Y. Min, W. Yang, Y. Lian, L. Lin, K. Feng, Z. Deng, M. Chen, J. Zhong, L. Xu, Y. Peng, Morphological and electronic tuning of Ni₂P through iron doping toward highly efficient water splitting, *ACS Catal.* 9 (2019) 8882–8892.
- [39] H. Zhao, D. Lu, J. Wang, W. Tu, D. Wu, S.W. Koh, P. Gao, Z.J. Xu, S. Deng, Y. Zhou, B. You, H. Li, Raw biomass electroreforming coupled to green hydrogen generation, *Nat. Commun.* 12 (2021) 2008.
- [40] N. Jiang, B. You, R. Boomstra, I.M. Terrero Rodriguez, Y. Sun, Integrating electrocatalytic 5-hydroxymethylfurfural oxidation and hydrogen production via Co-P-derived electrocatalysts, *ACS Energy Lett.* 1 (2016) 386–390.
- [41] H. Huang, C. Yu, X. Han, H. Huang, Q. Wei, W. Guo, Z. Wang, J. Qiu, Ni, Co hydroxide triggers electrocatalytic production of high-purity benzoic acid over 400 mA cm⁻², *Energy Environ. Sci.* 13 (2020) 4990–4999.
- [42] Y. Liu, C.L. Dong, Y.C. Huang, Y. Zou, Z. Liu, Y. Liu, Y. Li, N. He, J. Shi, S. Wang, Identifying the geometric site dependence of spinel oxides for the electrooxidation of 5-hydroxymethylfurfural, *Angew. Chem. Int. Ed.* 59 (2020) 19215–19221.
- [43] N. Zhang, Y. Zou, L. Tao, W. Chen, L. Zhou, Z. Liu, B. Zhou, G. Huang, H. Lin, S. Wang, Electrochemical oxidation of 5-hydroxymethylfurfural on nickel nitride/carbon nanosheets: reaction pathway determined by *in situ* sum frequency generation vibrational spectroscopy, *Angew. Chem. Int. Ed.* 58 (2019) 15895–15903.
- [44] L. Yan, B. Zhang, J. Zhu, Y. Li, P. Tsakaras, P. Kang Shen, Electronic modulation of cobalt phosphide nanosheet arrays via copper doping for highly efficient neutral-pH overall water splitting, *Appl. Catal. B Environ.* 265 (2020), 118555.